



PAPER

High-resolution x-ray spectra of carbon monoxide reveal ultrafast dynamics induced by long UV pulse

OPEN ACCESS

RECEIVED

11 February 2021

REVISED

19 April 2021

ACCEPTED FOR PUBLICATION

14 May 2021

PUBLISHED

11 June 2021

Original content from this work may be used under the terms of the [Creative Commons Attribution 4.0 licence](https://creativecommons.org/licenses/by/4.0/).

Any further distribution of this work must maintain attribution to the author(s) and the title of the work, journal citation and DOI.



Ji-Cai Liu^{1,*} , Viktoriia Savchenko^{2,3} , Victor Kimberg^{2,3,*} , Faris Gel'mukhanov^{2,3,4,5}  and Michael Odelius⁶ 

¹ Department of Mathematics and Physics, North China Electric Power University, 102206 Beijing, People's Republic of China

² Department of Theoretical Chemistry and Biology, KTH Royal Institute of Technology, 10691 Stockholm, Sweden

³ International Research Center of Spectroscopy and Quantum Chemistry – IRC SQC, Siberian Federal University, 660041 Krasnoyarsk, Russia

⁴ Kirensky Institute of Physics, Federal Research Center KSC SB RAS, 660036 Krasnoyarsk, Russia

⁵ Institute for Methods and Instrumentation in Synchrotron Radiation Research FG-ISRR, Helmholtz-Zentrum Berlin für Materialien und Energie, Albert-Einstein-Strasse 15, 12489 Berlin, Germany

⁶ Department of Physics, AlbaNova University Center, Stockholm University, SE-106 91 Stockholm, Sweden

* Authors to whom any correspondence should be addressed.

E-mail: jicailiu@ncepu.edu.cn and kimberg@kth.se

Keywords: UV pump—x-ray probe, molecular spectroscopy, ultrafast dynamics, potential energy surfaces, x-ray absorption

Abstract

In theoretical simulations of a UV + x-ray pump-probe (UVX-PP) setup, we show that frequency detuning of the pump UV pulse acts as a camera shutter by regulating the duration of the UVX-PP process. This two-photon absorption with long overlapping UV and x-ray pulses, allowing for high spectral resolution, thereby provides information about ultrafast dynamics of the nuclear wave packet without the requirement of ultrashort pulses and controlled delay times.

In a case study of carbon monoxide, the calculated UVX-PP spectra of the $O1s^{-1}2\pi^1$ and $C1s^{-1}2\pi^1$ core-excited states show different vibrational profiles. The interference of intermediate vibrational states reveals details of nuclear dynamics in the UVX-PP process related to a variable duration time controlled by the UV detuning. Both $O1s^{-1}2\pi^1$ and $C1s^{-1}2\pi^1$ pump-probe channels display a splitting of the spectral profile, which however is associated with different physical mechanisms. At the $O1s^{-1}2\pi^1$ resonance, the observed dispersive and non-dispersive spectral bands intersect and result in destructive interference.

1. Introduction

Pump-probe spectroscopy invented in optical laser physics is often associated with measurements with high time-resolution achieved with ultrashort laser pulses [1], but can be set-up to operate with both long [2] and short [3] laser pulses to get spectral resolution. Due to the fast development of laser technology in the x-ray region, pump-probe spectroscopy is moving rapidly into the short wavelengths region [4–7]. Usually infrared (IR), optical or ultraviolet (UV) pulses are used as the pump while time delayed IR [8] or x-ray pulses from a synchrotron [9], higher harmonic generation [10] or a free-electron laser [11] then probe the pumped system. X-ray pump-x-ray probe spectra of high spectral resolution can be obtained even for short stochastic XFEL pulses with limited spectral coherence using the covariance-mapping technique [12]. Different theoretical schemes have been suggested in the past for IR + x-ray pump-probe spectroscopy [13–16]. Here we develop a general time-dependent theory of UV + x-ray pump-probe spectroscopy (UVX-PP) for long overlapping UV and x-ray pulses and apply this to the CO molecule. Experimental and theoretical studies of UV absorption spectra of carbon monoxide has been performed in references [17–19].

The physics of the studied two-photon UVX-PP process is closely analogous to resonant inelastic x-ray scattering (RIXS) and resonant Auger scattering [20, 21]. The inverted analogue of the UVX-PP process—RIXS—has been studied theoretically and experimentally near the $C1s \rightarrow 2\pi$ [22, 23] and $O1s \rightarrow 2\pi$ [24, 25] core-excitations in CO. Due to strong overlap of the $A^1\Pi(5\sigma^{-1}2\pi^1)$ RIXS transition with

another close lying transition, one cannot investigate the pure $A^1\Pi$ RIXS band. The UVX-PP process gives opportunity to study nuclear dynamics in the $A^1\Pi$ state alone even when using long pulses which preserve spectral resolution.

Ultrafast time-resolved measurements of femtosecond (fs) nuclear dynamics can be performed in two ways. The direct way uses the time delayed short pump and probe pulses. However, the usage of short pulses leads to poor spectral resolution in accordance with the energy-time uncertainty principle. As we show here, there is an alternative indirect technique to control the nuclear dynamics making use of long pulses and, hence, preserve high spectral resolution. This method is based on a pure quantum concept, the ‘duration time’ of the UVX-PP process,

$$\tau = \frac{1}{\sqrt{\Omega_{UV}^2 + \gamma^2}}. \quad (1)$$

In this case, timing of the UVX-PP process is possible via variation of the frequency detuning Ω_{UV} from the UV pump transition. The resulting duration time is characterized by an irreversible quenching of the propagation in the intermediate state with the rate γ and the detuning Ω_{UV} which selectively quenches the long time contribution to UVX-PP amplitude due to dephasing.

This paper is organized as follows. In section 2, we present the physical model of the studied UVX-PP process taking into account the nuclear degrees of freedom of molecule using a time-dependent wave packet technique. Computational details and the discussion of obtained results are collected in section 3. The formation of resonant and non-resonant UVX-PP spectral bands is discussed in section 3.1. Section 3.2 is devoted to the dynamics of the pump-probe process and to analysis of the spectral peculiarities of the UVX-PP cross-section. Our findings are summarized in section 4.

2. Theory/dynamical theory of UVX-PP process

We shall begin with the brief outline of our model and the theoretical tools used in the article. The molecules interact with electric fields associated with the long overlapping UV and x-ray pulses

$$\mathcal{E}_{UV} = \frac{1}{2}E_{UV}\mathbf{e}_{UV}e^{i\omega_{UV}t} + \text{c.c.}, \quad \mathcal{E}_X = \frac{1}{2}E_X\mathbf{e}_Xe^{i\omega_Xt} + \text{c.c.} \quad (2)$$

The UV pulse which pumps the molecule from the ground electronic state ϕ_0 to the valence-excited state ϕ_1 is characterized by its amplitude E_{UV} , polarization vector \mathbf{e}_{UV} , and frequency ω_{UV} . The vibrational wave packet created by the pump is probed by an x-ray field (E_X , \mathbf{e}_X , ω_X) which promotes the molecule into a core-excited state ϕ_2 . The theory of this process is very similar to the description of RIXS [20, 26, 27]. Therefore we can write directly the expression for the cross-section of the UVX-PP process

$$\begin{aligned} \sigma &= \varrho\sigma_{\text{nucl}}, \quad \varrho \propto \overline{(\mathbf{e}_{UV} \cdot \mathbf{d}_{01})(\mathbf{e}_X \cdot \mathbf{d}_{12})}^2, \\ \sigma_{\text{nucl}} &= \sum_{\nu_2} |F_{\nu_2}|^2 \Delta(\omega_{UV} + \omega_X - \omega_{20} - \epsilon_{\nu_2} + \epsilon_0, \Gamma), \\ F_{\nu_2} &= \sum_{\nu_1} \frac{\langle 0_0 | \nu_1 \rangle \langle \nu_1 | \nu_2 \rangle}{\omega_{UV} - \omega_{10} - \epsilon_{\nu_1} + \epsilon_0 + i\gamma}. \end{aligned} \quad (3)$$

The polarization prefactor ϱ depends on the scalar product of polarization vectors and the transition dipole moments of UV (\mathbf{d}_{01}) and x-ray (\mathbf{d}_{12}) transitions. The overline represents averaging over random orientations of molecules in gas or liquid phases [26]. The studied process depends on the Franck–Condon (FC) amplitudes $\langle \nu_n | \nu_m \rangle$ or overlap between vibrational states $|\nu_n\rangle$ and $|\nu_m\rangle$. Here $\omega_{mn} = U_m^{\text{min}} - U_n^{\text{min}}$ is the resonant frequency between the bottom of the potential wells of the m th and n th electronic states, ϵ_{ν_n} is the energy of the ν_n th vibrational level of electronic state ϕ_n ($n = 0, 1, 2$), $\epsilon_0 = \omega_0^{(0)}/2$ is the zero-point vibrational energy, γ and Γ are the lifetime broadenings (half-width half-maximum—(HWHM) of the valence and core-excited states, respectively, and $\Delta(\Omega, \Gamma) = \Gamma/\pi(\Omega^2 + \Gamma^2)$.

The nuclear part of the UVX-PP cross-section (3) can be rewritten in a time-dependent representation [28–30] which is the main tool in our simulations

$$\begin{aligned}\sigma_{\text{nucl}} &= \frac{1}{\pi} \text{Re} \int_0^{\infty} dt \sigma(t) e^{i(\omega_{\text{UV}} + \omega_{\text{X}} - \omega_{20} + \epsilon_0 + i\Gamma)t}, \\ \sigma(t) &= \langle \Psi(0) | \Psi(t) \rangle, \quad |\Psi(t)\rangle = e^{-ih_2 t} |\Psi(0)\rangle, \\ |\Psi(0)\rangle &= \int_0^{\infty} dt e^{-\frac{t}{\tau_C}} |\psi_1(t)\rangle, \quad |\psi_1(t)\rangle = e^{-ih_1 t} |0_0\rangle,\end{aligned}\quad (4)$$

where $h_n = K + U_n(R) - U_n^{\text{min}}$ is the nuclear Hamiltonian of the n th electronic state. The time-dependent representation (4) has two main advantages in comparison with the time-independent equation (3). The former one is numerically advantageous in the case of high-density of excited vibrational states or when dissociative states are involved in the process [7, 20]. However, the most outstanding feature of the time-dependent approach, it that it gives insight in the dynamics of studied coherent process characterized by the complex time

$$\tau_C = \frac{1}{\gamma - i(\omega_{\text{UV}} - \omega_{10} + \epsilon_0)}. \quad (5)$$

The absolute value of this time $\tau = |\tau_C|$ (see equation (1)) determines the duration of the UVX-PP process which provides a unique opportunity to control the extent of dynamics by varying the detuning Ω_{UV} . The role of the detuning is seen from the integrand, $\exp(-t/\tau_C) = \exp(i\Omega_{\text{UV}}t)\exp(-\gamma t)$, of the wave packet $|\Psi(0)\rangle$ (4). The dephasing oscillations ($\exp(i\Omega_{\text{UV}}t)$) with frequency Ω_{UV} quench long-time contributions in $|\Psi(0)\rangle$.

Before concluding this section, we should notice that the dynamics of the UVX-PP process is sensitive to spectral shape of the UV absorption [28–30] $\phi_0 \rightarrow \phi_1$

$$\begin{aligned}\sigma_{\text{nucl}}^{\text{abs}} &= \frac{1}{\pi} \text{Re} \int_0^{\infty} dt \sigma_1(t) e^{i(\omega_{\text{UV}} - \omega_{10} + \epsilon_0 + i\gamma)t}, \\ \sigma_1(t) &= \langle 0_0 | \psi_1(t) \rangle,\end{aligned}\quad (6)$$

as well as to the x-ray absorption $\phi_0 \rightarrow \phi_2$, which is defined by the same equation after replacement of the UV frequency by an x-ray frequency ($\omega_{\text{UV}} \rightarrow \omega_{\text{X}}$), the valence-excited state by the core-excited state ($\phi_1 \rightarrow \phi_2$), and a corresponding replacement of the lifetime-broadening: $\gamma \rightarrow \Gamma$.

3. Results and discussion

To compute the cross sections we use the time-dependent wave packet technique that is an efficient framework for describing the nuclear dynamics. The evolution of the nuclear wave packet is obtained by solving directly the time-dependent Schrödinger equation in Cartesian coordinates with a split-time operator algorithm [31, 32].

To demonstrate the theory of UVX-PP in a case study, let us consider the CO molecule which has an electronic ground state $|X^1\Sigma^+\rangle = |O1s^2C1s^2 \dots 4\sigma^2 1\pi^4 5\sigma^2\rangle$, and the UV field pumps the first excited state $A^1\Pi(5\sigma^{-1}2\pi^1)$ by excitation of an electron from the highest occupied molecular orbital (HOMO) to the lowest unoccupied molecular orbital. For the combination with the x-ray pulse, we have two possible schemes shown in figure 1.

One should notice that in studied region of UV absorption ($\omega_{\text{UV}} \approx 8$ eV) we have 3 close lying states [24, 25] $A^1\Pi(5\sigma^{-1}2\pi^1)$, $I^1\Sigma^-(1\pi^{-1}2\pi^1)$, $D^1\Delta(1\pi^{-1}2\pi^1)$. However, UV transitions from ground state $|X^1\Sigma^+\rangle \rightarrow |I^1\Sigma^-\rangle$ and $|X^1\Sigma^+\rangle \rightarrow |D^1\Delta\rangle$ are forbidden because $+\rightarrow-$ and $\Sigma \rightarrow \Delta$ transitions are dipole forbidden (contrary to RIXS [24, 25]).

First UVX-PP channel (figure 1(a)) has the same core-orbital to valence-orbital transition $O1s \rightarrow 2\pi$ as the ordinary XAS transition from ground state and, hence, approximately similar resonant energy. This makes it difficult to distinguish the UVX-PP and ground state x-ray absorption.

Therefore we focus in our study on the second UVX-PP channel (figure 1(b)) where the UV field again creates the hole in HOMO 5σ . Then the x-ray photon fills this valence hole by exciting the core-electron $O1s \rightarrow 5\sigma$. Since the energy of this x-ray transition is smaller by about 8 eV than the main x-ray transition $O1s \rightarrow 2\pi$ (see table 1), the UVX-PP signal is not masked by ground state absorption. We consider core-excitations at both the oxygen and carbon K -edges (involving $1s$ electrons in the $O1s$ and $C1s$

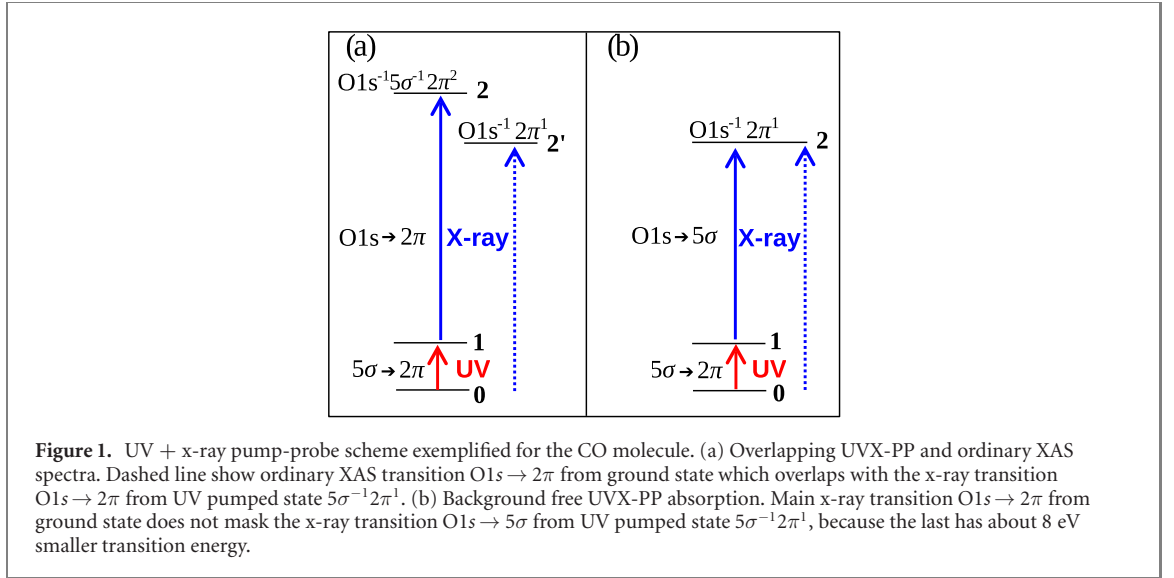


Figure 1. UV + x-ray pump-probe scheme exemplified for the CO molecule. (a) Overlapping UVX-PP and ordinary XAS spectra. Dashed line show ordinary XAS transition $O1s \rightarrow 2\pi$ from ground state which overlaps with the x-ray transition $O1s \rightarrow 2\pi$ from UV pumped state $5\sigma^{-1}2\pi^1$. (b) Background free UVX-PP absorption. Main x-ray transition $O1s \rightarrow 2\pi$ from ground state does not mask the x-ray transition $O1s \rightarrow 5\sigma$ from UV pumped state $5\sigma^{-1}2\pi^1$, because the last has about 8 eV smaller transition energy.

Table 1. Experimental parameters of the CO PECs of the ground state $X^1\Sigma^+$, core-excited states $O1s^{-1}2\pi^1$, $C1s^{-1}2\pi^1$, and the valence-excited state $A^1\Pi(5\sigma^{-1}2\pi^1)$. E_{00} is resonant energy of the $\nu = 0 \rightarrow \nu = 0$ transition. The reduced mass of CO is $\mu = 125.05.633$ a.u. All parameters are taken from references [22, 33], except Γ .

State	R_0 (a.u.)	ω_0 (meV)	$\omega_0 x_e$ (meV)	D (eV)	E_{00} (eV)	Γ (meV)	ζ (a.u.)
CO($X^1\Sigma^+$)	2.132	269	1.65	11.092	0	0	1.225
$O1s^{-1}2\pi^1$	2.419	176.81	2.33	3.358	533.4	79 [25]	1.462
$C1s^{-1}2\pi^1$	2.179	258.32	1.90	7.699	287.41	43 [34]	1.411
$A^1\Pi(5\sigma^{-1}2\pi^1)$	2.334	188.23	2.40	3.683	8.068	20	1.321

core-orbitals, respectively)

$$\begin{aligned} \omega_{UV} + |X^1\Sigma^+ \rangle &\rightarrow |A^1\Pi(5\sigma^{-1}2\pi^1) \rangle \rightarrow \omega_X + |A^1\Pi(5\sigma^{-1}2\pi^1) \rangle \rightarrow |O1s^{-1}2\pi^1 \rangle, \\ \omega_{UV} + |X^1\Sigma^+ \rangle &\rightarrow |A^1\Pi(5\sigma^{-1}2\pi^1) \rangle \rightarrow \omega_X + |A^1\Pi(5\sigma^{-1}2\pi^1) \rangle \rightarrow |C1s^{-1}2\pi^1 \rangle. \end{aligned} \quad (7)$$

We compute UVX-PP spectra (4) as the function of x-ray photon frequency ω_X for different UV excitation energies ω_{UV} . In the simulations, we use Morse potentials of CO (figure 2)

$$U(x) = D(1 - e^{-\zeta x})^2, \quad x = R - R_0 \quad (8)$$

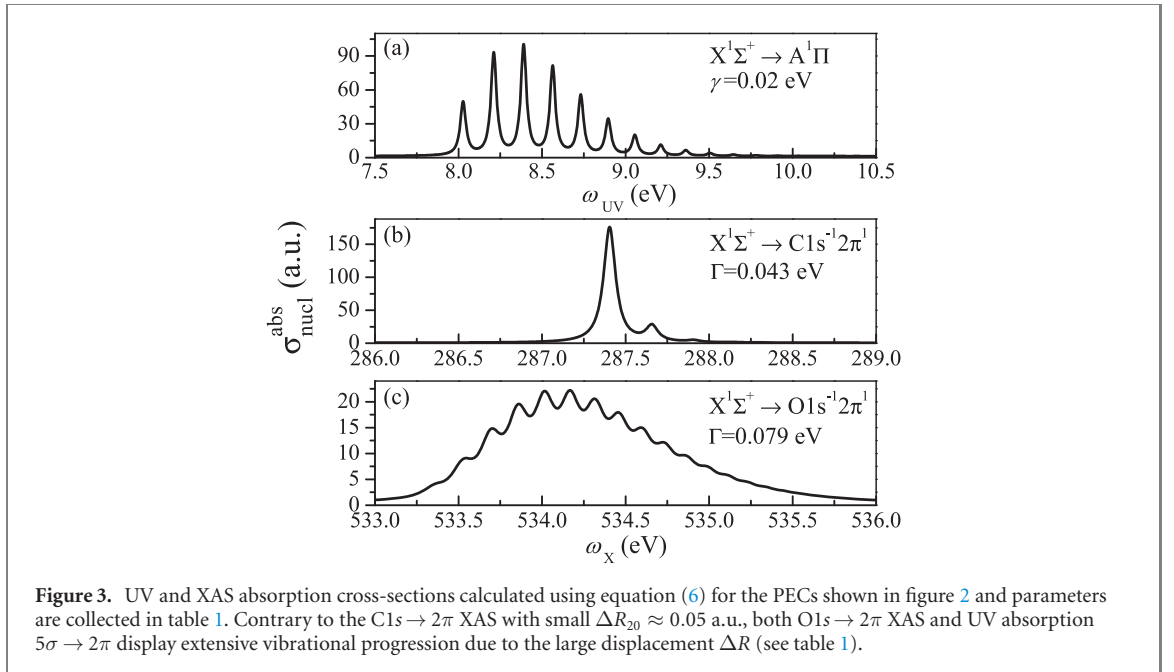
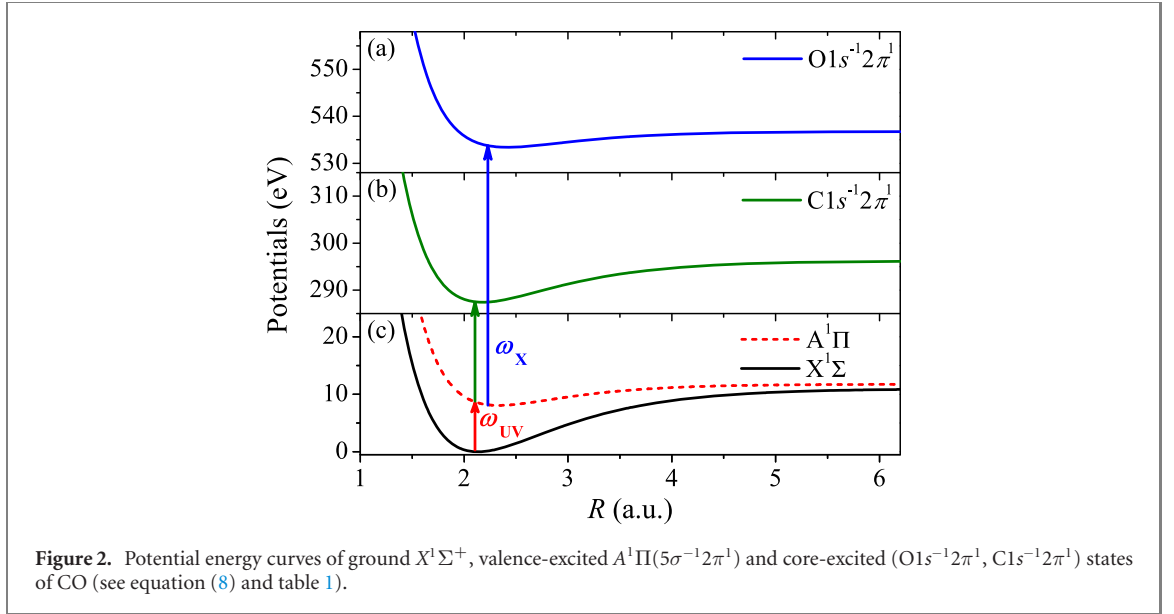
parameters of which were extracted from experiment (see table 1 which contains additional information).

Figure 3(a) (see equation (6)) shows that the UV absorption profile of CO has a rich vibrational structure due to the large displacement ($\Delta R_{10} \approx 0.20$ a.u.) of the minima of the excited state $A^1\Pi(5\sigma^{-1}2\pi^1)$ with respect to the ground state $X^1\Sigma^+$ seen in figure 2. A similarly broad vibrational profile can see for $O1s \rightarrow 2\pi$ XAS due to $\Delta R_{20} \approx 0.29$ a.u., in contrast with the weak vibrational features in $C1s \rightarrow 2\pi$ XAS which has a small $\Delta R_{20} \approx 0.05$ a.u..

3.1. Nuclear dynamics vs the UV detuning: resonant and non-resonant spectral bands

In close analogy with RIXS [20, 35] the studied UVX-PP process is characterized by the duration time (1) $\tau = |\tau_C|$ which one can vary by changing the detuning $\Omega_{UV} = \omega_{UV} - \omega_{10}$ from the UV resonance. In comparison with equation (5) we neglected here the not essential zero-point energy ϵ_0 . Similar to RIXS [20, 36, 37], equation (3) will correspond to a direct transition from the ground state to the final core-excited state $\phi_0 \rightarrow \phi_2$ when the detuning $|\Omega_{UV}|$ significantly exceeds the vibrational width HWHM $\Delta \sim 0.5$ eV of the UV absorption spectrum (figure 3(a)). This is confirmed in the simulations presented in figure 4 for $\Omega_{UV} = +3.0$ and approximately for -1.0 eV at both the carbon and oxygen K -edges:

$$\begin{aligned} F_{\nu_2} &\approx \frac{1}{\Omega_{UV}} \sum_{\nu_1} \langle 0_0 | \nu_1 \rangle \langle \nu_1 | \nu_2 \rangle = \frac{\langle 0_0 | \nu_2 \rangle}{\Omega_{UV}}, \quad |\Omega_{UV}| \gg \Delta, \\ \sigma_{\text{nucl}} &\approx \frac{1}{\Omega_{UV}^2} \sum_{\nu_2} |\langle 0_0 | \nu_2 \rangle|^2 \times \Delta(\omega_{UV} + \omega_X - \omega_{20} - \epsilon_{\nu_2} + \epsilon_0, \Gamma). \end{aligned} \quad (9)$$

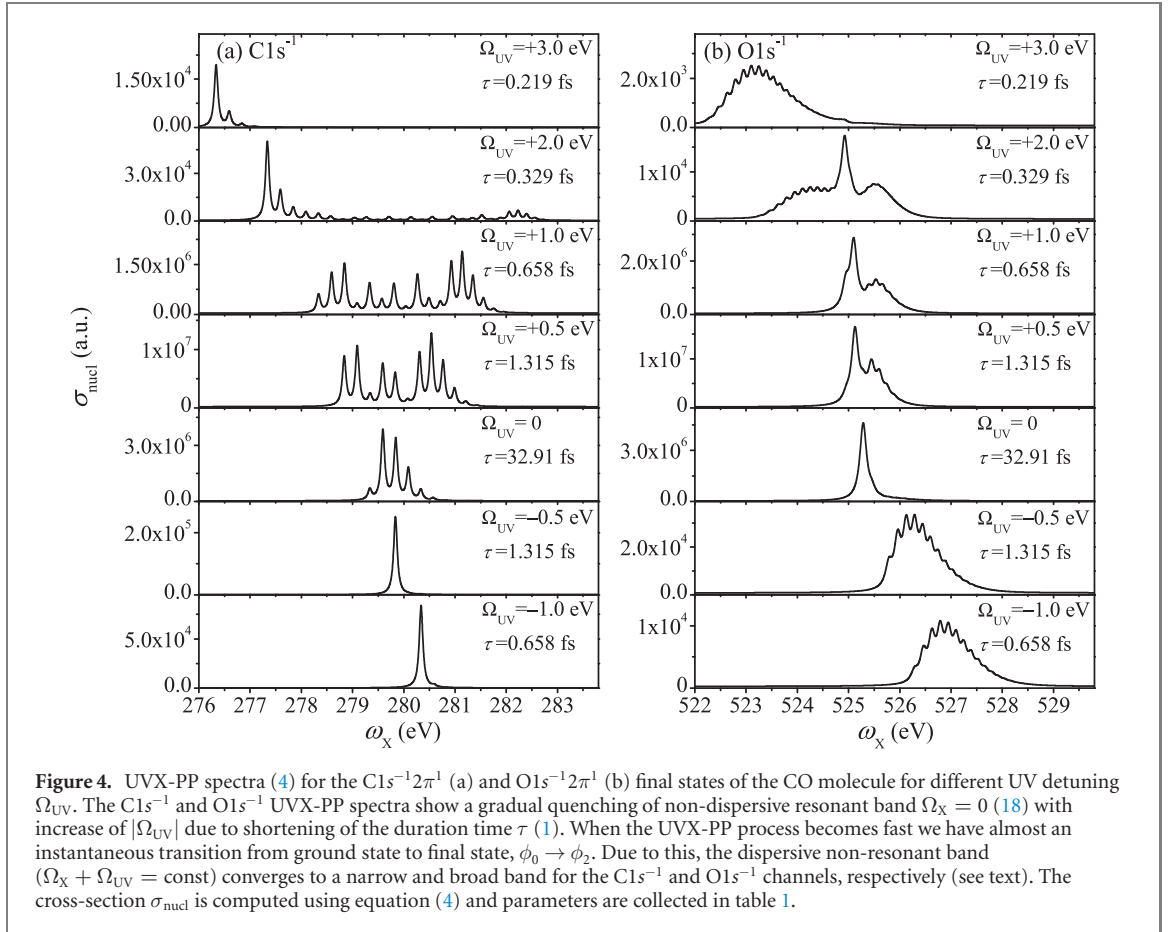


This spectrum exactly copies the XAS profile $\phi_0 \rightarrow \phi_2$. The physical reason for this is that because of short duration (1) of the process in the limit $|\Omega_{UV}| \gg \Delta$, the intermediate state, 1, has not time to be populated and the population is transferred instantaneously to the final core-excited state, 2. To accentuate the dynamical origin of the asymptote (9) let us take the short-time ($\tau \approx |\Omega_{UV}|^{-1} \ll \Delta^{-1}$) asymptote of the wave packet $|\Psi(0)\rangle$ (4)

$$|\Psi(0)\rangle = \int_0^\infty dt e^{-\frac{t}{\tau_c}} |\psi_1(t)\rangle \approx |\psi_1(0)\rangle \int_0^\infty dt e^{-\frac{t}{\tau_c}} = \tau_c |0_0\rangle, \quad \tau\Delta \ll 1. \quad (10)$$

This asymptote of a fast UVX-PP process shows that the initial wave packet $|\Psi(0)\rangle$ for the wave packet in final core-excited state $|\Psi(t)\rangle$ (3) is the lowest vibrational state $|0_0\rangle$ of the ground electronic state instead of nuclear wave packet $|\psi_1(t)\rangle$ which is affected by the nuclear dynamics in the intermediate valence-excited state for a finite time, t . The cross-section (9) shows that in the asymptotic limit of fast two-photon absorption (large $|\Omega_{UV}|$), the center of gravity of UVX-PP band follows the anti-Raman dispersion law in full agreement with the wave packet simulations (figure 4)

$$\omega_X = -\omega_{UV} + \omega_{20} + \epsilon_V^{(2)} - \epsilon_0, \quad (11)$$



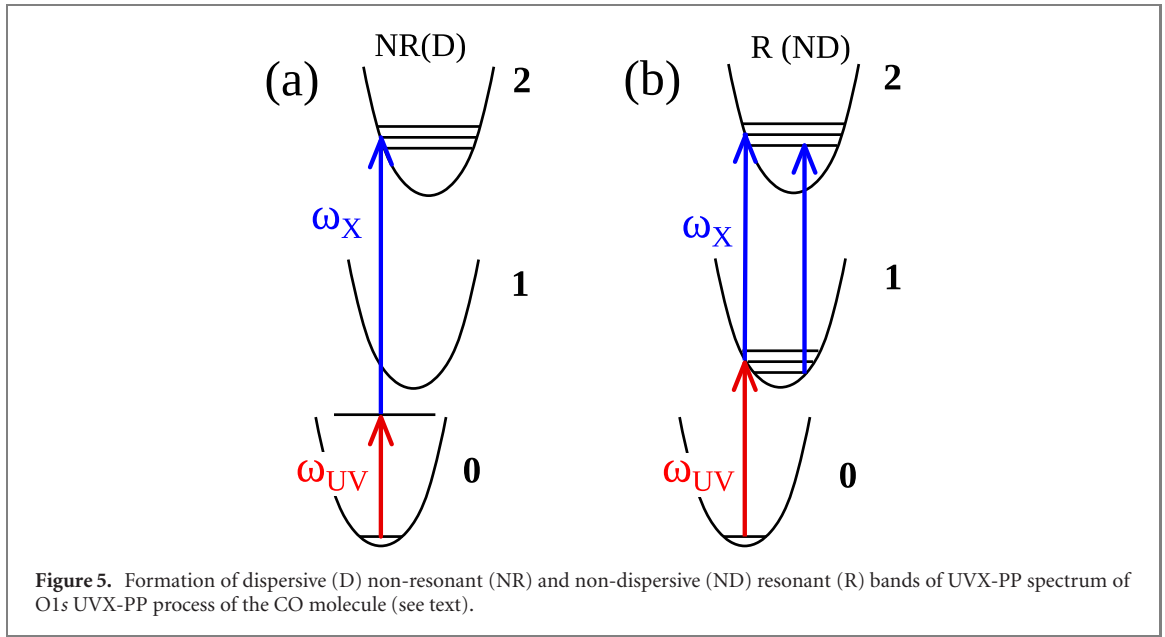
where $\epsilon_V^{(2)}$ is the nuclear energy of the core-excited state at the point $R_0^{(0)}$ of the vertical transition $\phi_0 \rightarrow \phi_2$. To emphasize the off-resonant nature of this limit this is denoted as a non-resonant (NR) UVX-PP process (figure 5).

The dynamics of the studied process is defined by shifts of minima of the potential energy curves (PEC) of CO molecule (see figure 2 and table 1)

$$\begin{aligned}
 \text{O: } \Delta R_{20} &= R_0^{(2)} - R_0^{(0)} \approx 0.29 \text{ a.u.}, \\
 \Delta R_{21} &= R_0^{(2)} - R_0^{(1)} \approx 0.08 \text{ a.u.}, \\
 \text{C: } \Delta R_{20} &= R_0^{(2)} - R_0^{(0)} \approx 0.05 \text{ a.u.}, \\
 \Delta R_{21} &= R_0^{(2)} - R_0^{(1)} \approx -0.16 \text{ a.u.}
 \end{aligned} \tag{12}$$

Large shift ΔR_{20} of the PECs' minima at the oxygen K -edge gives a broad FC distribution $|\langle 0_0 | \nu_2 \rangle|^2$ and explains the large width of the $O1s$ XAS spectrum (figure 3(c)) and, hence, also of the $O1s^{-1}$ UVX-PP spectrum (figure 4(b)) for large detuning. Situation is opposite for the $C1s$ XAS (figure 3(b)) and the $C1s^{-1}$ UVX-PP spectra (figure 4(a)), where the displacement ΔR_{20} is small. Here, similar to RIXS [20, 36, 37], we see in the $C1s^{-1}$ UVX-PP spectra (figure 4(a)) an almost complete collapse of the vibrational structure in the NR limit, since $\langle 0_0 | \nu_2 \rangle \approx \delta_{\nu_2 0_0}$.

The picture is qualitatively different for the slow UVX-PP process (1), $\tau \gg |\Omega_{UV}|^{-1}$ ($|\Omega_{UV}| \lesssim \Delta$). In this case of resonant (R) two-photon absorption (figure 5(b)) the intermediate state has the time to be populated and the spectral shape of the probe x-ray spectrum is defined by the overlap of vibrational states of intermediate and final electronic states $\langle \nu_1 | \nu_2 \rangle$. Due to the small shift ($\Delta R_{21} \approx 0.08$ a.u.) of PECs of the intermediate and final states (12) for the $O1s^{-1}$ UVX-PP process, we can probe transitions almost without change of the vibrational quantum number, $\langle \nu_1 | \nu_2 \rangle \approx \delta_{\nu_1, \nu_2}$ (see appendix A). This makes all emission transition energies almost the same (figure 5) because of the small anharmonicity and results in a collapse of the vibrational structure into a single peak in full agreement with the simulations (figure 4(b)). The situation is different for the $C1s^{-1}$ UVX-PP spectrum (figure 4(a)). Because now the shift $\Delta R_{21} \approx -0.16$ a.u. (12) is large, the vibrational quantum number changes significantly in the $\phi_1 \rightarrow \phi_2$ transition,



$\langle \nu_1 | \nu_2 \rangle \neq \delta_{\nu_1, \nu_2}$. This explains the long vibrational progression of the $C1s^{-1}$ UVX-PP spectrum (figure 4(a)) in the resonant region $|\Omega_{UV}| \lesssim \Delta$, where the studied two-photon absorption is slow, $\tau \gtrsim \Delta^{-1}$.

The evolution of the RIXS spectra [20, 24, 25, 36, 37] in the course of variation of the scattering duration time $\tau_X = 1/\sqrt{(\omega_X - \omega_{20})^2 + \Gamma^2}$

$$\begin{aligned} \omega_X + |X^1\Sigma^+ \rangle &\rightarrow |1\sigma^{-1}2\pi^1 \rangle \rightarrow \omega'_X + |A^1\Pi (5\sigma^{-1}2\pi^1) \rangle, \\ \omega_X + |X^1\Sigma^+ \rangle &\rightarrow |2\sigma^{-1}2\pi^1 \rangle \rightarrow \omega'_X + |A^1\Pi (5\sigma^{-1}2\pi^1) \rangle \end{aligned}$$

can be different as compared to the present case, because the intermediate and final states in RIXS process ($\omega_X + |0\rangle \rightarrow |2\rangle \rightarrow \omega'_X + |1\rangle$) are inverted with respect to the UVX-PP process (7), $\omega_{UV} + |0\rangle \rightarrow |1\rangle \rightarrow \omega_X + |1\rangle \rightarrow |2\rangle$. The $C1s$ RIXS spectra will differ from the $C1s$ UVX-PP spectra because of the large shift $\Delta R_{21} \approx -0.16$ a.u. of PECs of intermediate core-excited and final valence-excited states (see equation (12)). In contrast, the RIXS and UVX-PP spectra will be approximately the same for the $O1s$ channel, since the shift is small $\Delta R_{21} \approx 0.08$ a.u..

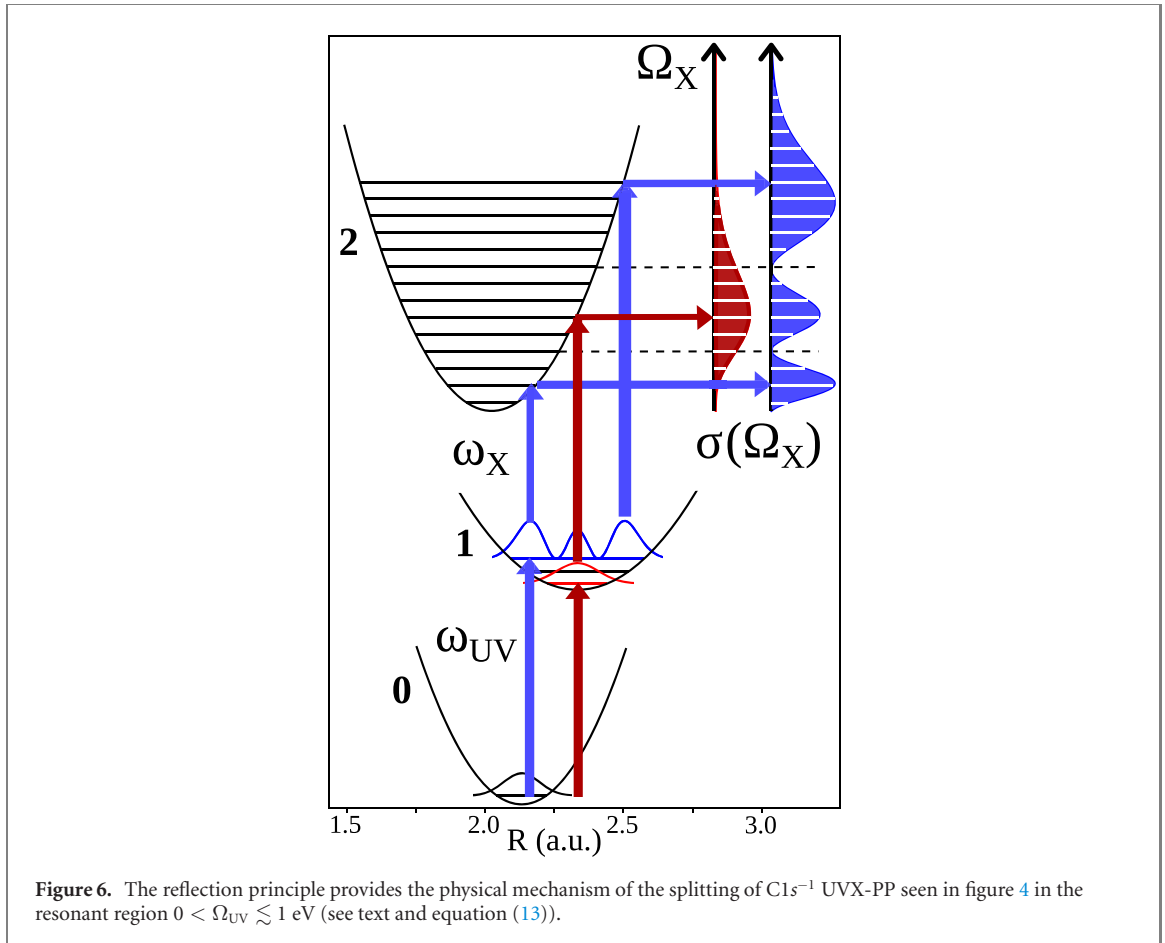
UVX-PP spectra give information about the PECs, which is complimentary to that from RIXS. For example, fast UVX-PP ($\tau\Delta \ll 1$) according to equation (9) allows to reconstruct the potential energy surface (PES) of the core-excited state from the experimental FC distribution $|\langle 0_0 | \nu_2 \rangle|^2$, while the fast RIXS (large $|\Omega_X|$) maps the potential of the valence excited state from the FC distribution $|\langle 0_0 | \nu_1 \rangle|^2$. A similar method is used in resonant photoemission [38, 39]. The dissociative intermediate state in the UVX-PP process allows to obtain one-dimensional cuts through the multidimensional PES of the final core-excited state similar to the method outlined for reconstruction of the PECs of the ground state using RIXS [40].

3.2. Details of evolution of UVX-PP profiles with variation of the UV detuning

In the previous section, we analyzed and explained the gross spectral features for slow and fast UVX-PP processes (small and large $|\Omega_{UV}|$), respectively. However, the development of spectral shapes of $C1s^{-1}$ and $O1s^{-1}$ UVX-PP profiles (figure 4) on the way to asymptotic region of large $|\Omega_{UV}|$ has additional spectral features, which we would like to discuss now.

3.2.1. $C1s$ UVX-PP

Contrary to negative UV detuning, figure 4(a) shows that the spectral profile develops a gradually increasing splitting at increasing Ω_{UV} from 0 to +1 eV. The occurrence of the splitting can be understood from the reflection principle illustrated in figure 6 taking into account the large shift $\Delta R_{10} \approx 0.20$ a.u. The one-dimensional reflection principle [38, 41–43] illustrated in figure 6 deserves a brief comment. According



to this principle the envelope of the UVX-PP cross-section for $\Omega_X = \omega_X - \omega_{21} \geq 0$

$$\sigma_{\text{nucl}}(\Omega_X) \approx |\psi_{\nu_1}(x(\Omega_X))|^2, \quad (13)$$

$$x(\Omega_X) = \frac{1}{\omega_0^{(2)}} \sqrt{\frac{2\Omega_X}{\mu}} + \Delta R_{21}$$

copies approximately the absolute square of the wave function $\psi_{\nu_1}(x)$ of the ν_1 th vibrational level pumped by UV field. The displacement (13) from equilibrium in the intermediate state $x(\Omega_X) = x = R - R_0^{(1)}$ is the solution of equation

$$\Omega_X = \frac{\mu(\omega_0^{(2)})^2}{2}(x - \Delta R_{21})^2 \quad (14)$$

for a harmonic potential of core-excited state 2.

As seen from the UV absorption spectrum (figure 3(a)), the increase of the detuning $\Omega_{UV} \geq 0$ leads to the successive population of the vibrational levels $\nu_1 = 0, 1, \dots, 7$. The wave function of the lowest vibrational level $\nu_1 = 0$ has one maximum and, according to the reflection principle, this results in one peak in the UVX-PP spectrum. However, the absolute square of the vibrational wave function of the UV excited vibrational level ϵ_{ν_1} shapes for two strong maxima near classical turning points when ν_1 increases with increasing Ω_{UV} . Hence, the change in shape of the vibrational wave packets for $\nu_1 = 1, \dots, 7$ in combination with the reflection principle (figure 6) explains the gradually increasing splitting of the UVX-PP spectrum with increasingly positive UV detuning (figure 4(a)). Such a splitting is not seen for negative detuning Ω_{UV} because of the absence of selective population of vibrational levels in the intermediate $A^1\Pi$ state. Furthermore, figure 4(a) shows that the center of gravity of this resonant band nearly does not depend on the detuning Ω_{UV} (see also below).

3.2.2. O1s UVX-PP: resonant (R) and non-resonant (NR) bands

The O1s UVX-PP profile (figure 4(b)) calculated using the wave packet approach (4) consists of two qualitatively different bands: one, broad, follows the anti-Raman dispersion law while the narrow peak is almost insensitive to the UV detuning Ω_{UV} .

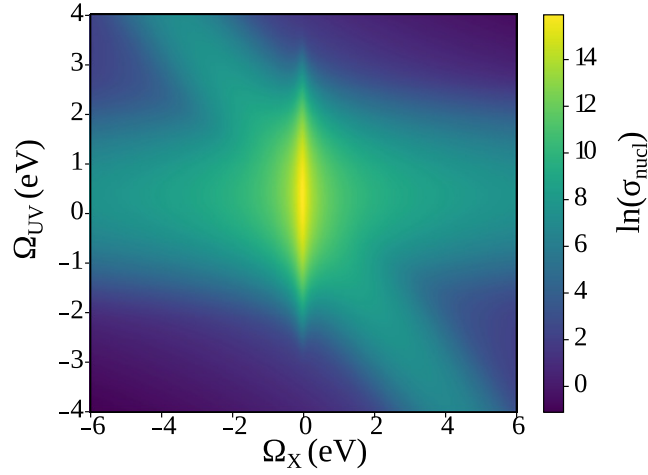


Figure 7. 2D map of the logarithm of O1s UVX-PP cross-section (16). Non-dispersive horizontal broad band is the Lorentzian tail $1/\Omega_X^2$ of the band (17), while the broad non-resonant band (19) exhibits anti-Raman dispersion (diagonal) (see equation (20)). $\hat{\Delta} = 0.7$ eV, $\gamma = 20$ meV, $\Gamma = 79$ meV, σ_{nucl} is computed in a.u..

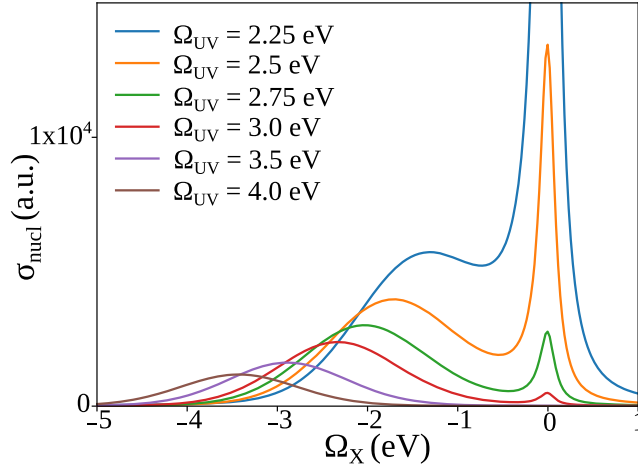
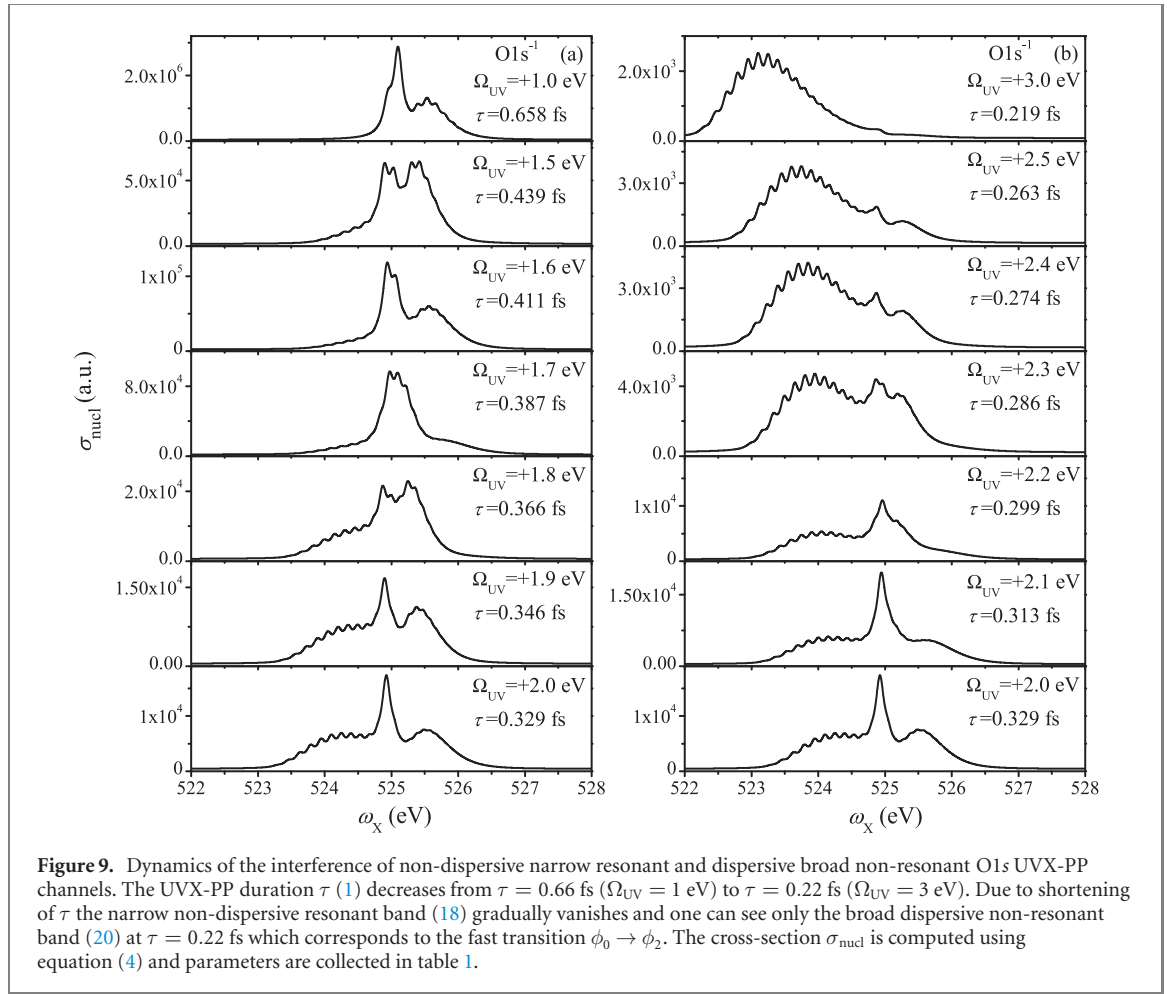


Figure 8. The region of the overlap of narrow resonant (R) and broad non-resonant (NR) O1s UVX-PP bands from figure 7. The position ($\Omega_X = 0$) of the resonant peak (18) does not depend on the UV detuning Ω_{UV} in contrast to the non-resonant band (19) which exhibits anti-Raman dispersion (20). $\hat{\Delta} = 0.7$ eV, $\gamma = 20$ meV, $\Gamma = 79$ meV.

The relative shifts ($\Delta R_{21} \approx 0.08$ a.u., $\Delta R_{20} \approx 0.29$ a.u.) of the equilibrium positions of the nuclei (12) in the O1s UVX-PP process provide a simple but still accurate model of the evolution of the O1s UVX-PP spectrum with variation of the UV detuning Ω_{UV} . Because ΔR_{21} is small (12) the following approximation for the FC amplitude $\langle \nu_1 | \nu_2 \rangle$ and hence, for the amplitude $F\nu_2$ (3), is applicable

$$\begin{aligned} \langle \nu_1 | \nu_2 \rangle &\approx \delta_{\nu_1, \nu_2}, \\ F\nu_2 &\approx \frac{\langle 0_0 | \nu_2 \rangle}{\Omega_{UV} - \epsilon_{\nu_2} + \epsilon_0 + i\gamma} \\ &\approx \left(\frac{1}{\pi \Delta^2} \right)^{1/4} \times \frac{\exp \left[-\frac{1}{2} \left(\frac{\epsilon - \epsilon_V^{(2)}}{\Delta} \right)^2 \right]}{\Omega_{UV} - \epsilon + \epsilon_0 + i\gamma}. \end{aligned} \quad (15)$$

One should mention that the FC amplitude $\langle \nu_1 | \nu_2 \rangle$ depends also on the change of the curvature of the PEC. However, the role of the change of the curvature is usually much smaller than ΔR_{21} (see appendix A). Due to a large shift ΔR_{20} , the O1s XAS spectrum $\phi_0 \rightarrow \phi_2$ has high density of states (figure 3(c)). This allows to consider the vibrational energy as a continuum variable $\epsilon_{\nu_2} \approx \epsilon$ and approximate the FC amplitude $\langle 0_0 | \nu_2 \rangle$ (15) by a Gaussian function [42, 44, 45]. This directly permits to write the UVX-PP



cross-section (3) in simple integral form (see figure 7 and figure 8)

$$\sigma_{nucl} = \frac{1}{\Delta\sqrt{\pi}} \int_{-\infty}^{\infty} d\epsilon \frac{\exp\left[-\left(\frac{\epsilon - \epsilon_V^{(2)}}{\Delta}\right)^2\right]}{(\Omega_{UV} - \epsilon + \epsilon_0)^2 + \gamma^2} \Delta(\Omega_{UV} + \Omega_X - \epsilon + \epsilon_0, \Gamma). \quad (16)$$

Here $\Omega_X = \omega_X - \omega_{21}$ and $\Delta = \tilde{\Delta}/\sqrt{\ln 2}$ where $\tilde{\Delta}$ is the HWHM of the O1s $\rightarrow 2\pi$ x-ray absorption spectrum. Let us look at the spectrum produced by equation (16) in a little more detail. As one can see from figures 3(a) and (c), the following inequality is valid for the O1s UVX-PP process

$$\Delta \gg \Gamma \gg \gamma.$$

The main contributions in the integral (16) come from the sharpest Lorentzian features ($\epsilon = \Omega_{UV} + \epsilon_0$ and $\epsilon = \Omega_{UV} + \Omega_X + \epsilon_0$)

$$\sigma_{nucl} \approx \frac{1}{\gamma\Delta\sqrt{\pi}} \left\{ \exp\left[-\left(\frac{\Omega_{UV} - (\epsilon_V^{(2)} - \epsilon_0)}{\Delta}\right)^2\right] \frac{\Gamma}{\Omega_X^2 + \Gamma^2} + \exp\left[-\left(\frac{\Omega_{UV} - (\epsilon_V^{(2)} - \epsilon_0) + \Omega_X}{\Delta}\right)^2\right] \frac{\gamma}{\Omega_X^2 + \gamma^2} \right\}. \quad (17)$$

When the UV frequency is tuned within the UV absorption band $|\Omega_{UV} - \epsilon_V^{(2)}| \lesssim \Delta$ the Ω_X dependence of the cross-section comes from narrow Lorentzians which describe a non-dispersive peak

$$\Omega_X = 0 \quad (18)$$

in agreement with figure 4(b) and strict computation of the integral (16) shown in figure 8.

When we instead detune the UV frequency beyond the strong UV absorption $|\Omega_{UV} - \epsilon_V^{(2)}| > \Delta$, then the first term in equation (17) decreases exponentially. Because the Gaussian decays much faster than the Lorentzian, the dominant contribution in (17) is now given by the second Gaussian

$$\sigma_{\text{nucl}} \approx \frac{1}{(\Omega_{UV} - \epsilon_V^{(2)})^2 \Delta \sqrt{\pi}} \exp \left[- \left(\frac{\Omega_{UV} - (\epsilon_V^{(2)} - \epsilon_0) + \Omega_X}{\Delta} \right)^2 \right]. \quad (19)$$

This expression corresponds to the fast UVX-PP process ($\tau\Delta \ll 1$) and explains the broad peak which exhibits anti-Raman dispersion

$$\Omega_X = -\Omega_{UV} + (\epsilon_V^{(2)} - \epsilon_0), \quad (20)$$

as seen in figures 4(b) and 8. As visualized in the 2D color map of $\ln(\sigma_{\text{nucl}})$ (figure 7), equation (16) captures the splitting of the UVX-PP profile into a narrow non-dispersive resonant (R) band and a broad dispersive NR band (19), in full agreement with general asymptotic behavior (9). This result is the source of another interesting dynamical aspect of the studied process; namely, that in the fast limit the UVX-PP profile coincides with the shape of the XAS $\phi_0 \rightarrow \phi_2$ as noticed above (see equation (9) and figure 3).

The R (18) and NR (20) bands intersect due to different dispersion and interfere in the region of the overlap as it shown in figure 8. The law of dispersion of the resonant band $\Omega_X = \text{const}$ and dispersion of the NR band, $\Omega_X + \Omega_{UV} = \text{const}$, provided by the model (16) is strict (9) only for a fast NR process ($\tau\Delta \ll 1$). However, the dispersion of the resonant band can in the general case strongly deviate [46] from $\Omega_X = \text{const}$ (18).

The model, presented in figure 8, reproduces the qualitative behavior of the strict wave packet simulations of O1s UVX-PP spectra shown in figure 4(b). There is a difference between the model (figure 8) and the strict result (see figures 4(b) and 9) where the interference is seen at the middle of the broad dispersive NR band. This bound-bound interference between the R and NR channels is reminiscent of the continuum-continuum interference [28, 47] where the interference occurs in the region of intersection of dispersive and non-dispersive spectral bands.

4. Summary

Based on accurate theoretical spectrum simulations, we propose a scheme for UV + x-ray pump-probe (UVX-PP) spectroscopy for long overlapping pulses. We show the formation of the two distinct vibrational bands (a non-dispersive band and a band that follows the anti-Raman dispersion law) which strongly depends on the duration of the UVX-PP process as controlled by detuning of pump pulse from the UV resonance. Due to different dispersion these bands intersect and interfere. The general theory is exemplified by the CO molecule. The time-dependent wave packet calculations show that evolution of C1s and O1s UVX-PP spectra with variation of the UV detuning is due to qualitatively different nuclear dynamics caused by different displacements of the PEC of the involved electronic states. The observed splitting in the C1s UVX-PP spectra is explained using the reflection principle. It is found that the UVX-PP spectra differ qualitatively from RIXS owing to inverted intermediate and final states. Because of this, these techniques give the complementary information about the PEC of valence- and core-excited states.

Acknowledgments

The reported study was funded by RFBR, project number 19-29-12015. J-CL thanks the support by the National Science Foundation of China under Grant Nos. 11974108, 11574082, and the Fundamental Research Funds for the Central Universities (No. 2021MS046). MO acknowledges funding from the European Union's Horizon 2020 research and innovation programme under the Marie Skłodowska-Curie Grant Agreement No. 860553 and the Carl Tryggers Foundation (contract CTS18:285). FG acknowledges also the support from the Helmholtz Virtual Institute VI419 'Dynamic Pathways in Multidimensional Landscapes'. VK acknowledges the Swedish Research Council (VR 2019-03470). The calculations were partially enabled by resources provided by the Swedish National Infrastructure for Computing (SNIC) partially funded by the Swedish Research Council through Grant Agreement No. 2018-05973.

Data availability statement

The data that support the findings of this study are available upon reasonable request from the authors.

Appendix A. FC factor vs shift of the minima and change of the curvature of PECs

The FC amplitude $\langle \nu_1 | \nu_2 \rangle$ (see equation (15)) depends on shape of the PECs $U_1(R)$ and $U_2(R)$ of the electronic states ϕ_1 and ϕ_2 , respectively. The shape of the bound state is characterized mainly by the shift of equilibrium $\Delta R_{21} = R_0^{(2)} - R_0^{(1)}$ and difference ($\Delta\omega_{21} = \omega_0^{(2)} - \omega_0^{(1)}$) of the vibrational frequencies. The vibrational frequency $\omega_0^{(i)} = \sqrt{U_i''/\mu}$ is characterized by the curvature U_i'' at the minimum of $U_i(R)$. To avoid cumbersome expressions let us consider the simplest case $\nu_1 = 0$ which sheds light on the general problem. Let us compare the FC factors $\langle 0_0 | \nu_2 \rangle^2$ for the two cases ($\Delta\omega_{21} = 0, \Delta R_{21} \neq 0$) and ($\Delta\omega_{21} \neq 0, \Delta R_{21} = 0$) using equations for $\langle \nu_1 | \nu_2 \rangle$ in harmonic PECs [46]

$$\langle 0_0 | \nu_2 \rangle^2 = \begin{cases} e^{-S} \frac{S^{\nu_2}}{\nu_2!}, & \Delta\omega_{21} = 0, \\ \frac{(2m)!}{(m!)^2} \eta \zeta^{2m} & \nu_2 = 2m, \quad \Delta R_{21} = 0, \\ 0, & \nu_2 = 2m + 1, \quad \Delta R_{21} = 0, \end{cases} \quad (\text{A.1})$$

where

$$S = \frac{1}{2} \left(\frac{\Delta R_{21}}{a} \right)^2, \quad a = \frac{1}{\sqrt{\mu \omega_0^{(1)}}}, \quad (\text{A.2})$$

$$\zeta = \frac{1}{2} \left(\frac{\Delta\omega_{21}}{\omega_0^{(2)} + \omega_0^{(1)}} \right), \quad \eta = \frac{2\sqrt{\omega_0^{(2)}\omega_0^{(1)}}}{\omega_0^{(2)} + \omega_0^{(1)}} \sim 1.$$

We see, that the role of the displacement ΔR_{21} and the change of curvature is characterized by the Huang–Rhys parameter S and the relative frequency difference ζ , respectively. In many cases, the Huang–Rhys parameter $S \gtrsim 1$ because the displacement ΔR_{21} is quite often comparable or larger than the amplitude of zero-point vibrations, a . In contrast, the difference $|\Delta\omega_{21}| \ll \omega_0^{(2)} + \omega_0^{(1)}$. For example, $\zeta \lesssim 0.1$ according to the experimental data [33] for the O_2 , CO and N_2 molecules. Thus, according to equation (A.1) this means that the displacement ΔR_{21} plays dominant role in FC factor in comparison with the change of the curvature, characterized by $\Delta\omega_{21}$.

ORCID iDs

Ji-Cai Liu  <https://orcid.org/0000-0002-4341-4823>

Viktoriiia Savchenko  <https://orcid.org/0000-0002-4792-9525>

Victor Kimberg  <https://orcid.org/0000-0003-1269-8760>

Faris Gel'mukhanov  <https://orcid.org/0000-0002-8272-7670>

Michael Odelius  <https://orcid.org/0000-0002-7023-2486>

References

- [1] González-Castrillo A, Palacios A, Bachau H and Martín F 2012 Clocking ultrafast wave packet dynamics in molecules through UV-induced symmetry breaking *Phys. Rev. Lett.* **8** 063009
- [2] Iparraguirre I, Aramburu I, Azkargorta J, Illarramendi M A, Fernández J and Balda R 2005 Wavelength tuning of titanium sapphire laser by its own crystal birefringence *Opt. Express* **13** 1254
- [3] Seto K, Yamada H, Kobayashi T and Tokunaga E 2019 Demonstration of wavelength-scan-free action spectroscopy in pump/probe measurement with supercontinuum pump light *Opt. Express* **27** 6976
- [4] Kowalewski M, Bennett K and Mukamel S 2017 Monitoring nonadiabatic avoided crossing dynamics in molecules by ultrafast x-ray diffraction *Struct. Dyn.* **4** 054101
- [5] Mincigrucci R, Kowalewski M, Rouxel J R, Bencivenga F, Mukamel S and Masciovecchio C 2018 Impulsive UV-pump/x-ray probe study of vibrational dynamics in glycine *Sci. Rep.* **8** 15466
- [6] Young L et al 2018 Roadmap of ultrafast x-ray atomic and molecular physics *J. Phys. B: At. Mol. Opt. Phys.* **51** 032003
- [7] Gel'mukhanov F, Odelius M, Polyutov S, Föhlisch A and Kimberg V 2021 Dynamics of resonant x-ray and Auger scattering *Rev. Mod. Phys.* (at press)
- [8] Carroll L, Friedli P, Lerch P, Schneider J, Treyer D, Hunziker S, Stutz S and Sigg H 2011 Ultra-broadband infrared pump-probe spectroscopy using synchrotron radiation and a tuneable pump *Rev. Sci. Instrum.* **82** 063101
- [9] Burian M, Marmiroli B, Radeticchio A, Morello C, Naumenko D, Biasiol G and Amenitsch H 2020 Picosecond pump-probe x-ray scattering at the eletra saxs beamline *J. Synchrotron Radiat.* **27** 51
- [10] Johnson A S, Avni T, Larsen E W, Austin D R and Marangos J P 2019 Attosecond soft x-ray high harmonic generation *Phil. Trans. R. Soc. A* **377** 20170468
- [11] Savelyev E et al 2017 Jitter-correction for IR/UV-XUV pump-probe experiments at the FLASH free-electron laser *New J. Phys.* **19** 043009

- [12] Kimberg V and Rohringer N 2016 Stochastic stimulated electronic x-ray Raman spectroscopy *Struct. Dyn.* **3** 034101
- [13] Guimarães F F, Kimberg V, Felicissimo V C, Gel'mukhanov F, Cesar A and Ågren H 2005 Infrared-x-ray pump-probe spectroscopy of the NO molecule *Phys. Rev.* **72** 012714
- [14] Felicissimo V C, Guimarães F F, Cesar A, Gel'mukhanov F and Ågren H 2006 Proton transfer mediated by the vibronic coupling in oxygen core ionized states of glyoxalmonoxime studied by infrared-x-ray pump-probe spectroscopy *J. Phys. Chem. A* **110** 12805
- [15] Liu J-C, Velkov Y, Rinkevicius Z, Ågren H and Gel'mukhanov F 2008 Symmetry-forbidden x-ray Raman scattering induced by a strong infrared-laser field *Phys. Rev.* **77** 043405
- [16] Ignatova N et al 2017 Gradual collapse of nuclear wave functions regulated by frequency tuned x-ray scattering *Sci. Rep.* **7** 43891
- [17] Levelt P F, Ubachs W and Hogervorst W 1992 Extreme ultraviolet laser spectroscopy on CO in the 91–100 nm range *J. Chem. Phys.* **97** 7160
- [18] Lefebvre-Brion H and Eidelsberg M 2012 New experimental study and theoretical model of the extreme UV absorption spectrum of CO isotopologs *J. Mol. Spectrosc.* **271** 59
- [19] Majumder M, Sathyamurthy N, Lefebvre-Brion H and Vázquez G J 2012 Photoabsorption of carbon monoxide: a time-dependent quantum mechanical study *J. Phys. B: At. Mol. Opt. Phys.* **45** 185101
- [20] Gel'mukhanov F and Ågren H 1999 Resonant x-ray Raman scattering *Phys. Rep.* **312** 87–330
- [21] Feifel R et al 2004 Generalization of the duration-time concept for interpreting high-resolution resonant photoemission spectra *Phys. Rev. A* **69** 022707
- [22] Skytt P, Glans P, Gunnelin K, Guo J, Nordgren J, Luo Y and Ågren H 1997 Role of screening and angular distributions in resonant x-ray emission of CO *Phys. Rev. A* **55** 134
- [23] Skytt P, Glans P, Gunnelin K, Guo J and Nordgren J 1997 Lifetime-vibrational interference effects in the resonantly excited x-ray-emission spectra of CO *Phys. Rev. A* **55** 146
- [24] Couto R C et al 2016 Anomalously strong two-electron one-photon x-ray decay transitions in CO caused by avoided crossing *Sci. Rep.* **6** 20947
- [25] Couto R C et al 2016 Coupled electron-nuclear dynamics in resonant $1\sigma \rightarrow 2\pi$ x-ray Raman scattering of CO molecules *Phys. Rev. A* **93** 032510
- [26] Gel'mukhanov F and Ågren H 1994 Resonant inelastic x-ray scattering with symmetry-selective excitation *Phys. Rev. A* **49** 4378–89
- [27] Ament L J P, van Veenendaal M, Devereaux T P, Hill J P and van den Brink J 2011 Resonant inelastic x-ray scattering studies of elementary excitations *Rev. Mod. Phys.* **83** 705
- [28] Sałek P, Gel'mukhanov F and Ågren H 1999 Wave-packet dynamics of resonant x-ray Raman scattering: excitation near the $L_{II,III}$ edge of HCl *Phys. Rev. A* **59** 1147–59
- [29] Couto R C et al 2017 Selective gating to vibrational modes through resonant x-ray scattering *Nat. Commun.* **8** 14165
- [30] Vaz da Cruz V et al 2019 Nuclear dynamics in resonant inelastic x-ray scattering and x-ray absorption of methanol *J. Chem. Phys.* **150** 234301
- [31] Liu J-C, Kohler M C, Keitel C H and Hatsagortsyan K Z 2011 Coherent x-ray generation from below-threshold harmonics *Phys. Rev. A* **84** 063817
- [32] Feit M D, Fleck J A and Steiger A 1982 Solution of the Schrödinger equation by a spectral method *J. Comput. Phys.* **47** 412
- [33] Neeb M, Rubensson J-E, Biermann M and Eberhardt W 1994 Coherent excitation of vibrational wave functions observed in core hole decay spectra of O₂, N₂ and CO *J. Electron Spectrosc. Relat. Phenom.* **67** 261
- [34] Osborne S J, Ausmees A, Svensson S, Kivimäki A, Sairanen O P, de Brito A N, Aksela H and Aksela S 1995 The vibrationally resolved participator auger spectra of selectively excited $C1s(2\sigma)^{-1}2\pi^1$ vibrational states in carbon monoxide *J. Chem. Phys.* **102** 7317
- [35] Gel'mukhanov F, Sałek P, Privalov T and Ågren H 1999 Duration of x-ray Raman scattering *Phys. Rev. A* **59** 380–9
- [36] Gel'mukhanov F, Privalov T and Ågren H 1997 Collapse of vibrational structure in spectra of resonant x-ray Raman scattering *Phys. Rev. A* **56** 256–64
- [37] Sundin S, Gel'mukhanov F K, Ågren H, Osborne S J, Kikas A, Björneholm O, Ausmees A and Svensson S 1997 Collapse of vibrational structure in the auger resonant Raman spectrum of CO by frequency detuning *Phys. Rev. Lett.* **79** 1451
- [38] Miron C, Nicolas C, Travnikova O, Morin P, Sun Y, Gel'mukhanov F, Kosugi N and Kimberg V 2012 Imaging molecular potentials using ultrahigh-resolution resonant photoemission *Nat. Phys.* **8** 135
- [39] Kimberg V, Lindblad A, Söderström J, Travnikova O, Nicolas C, Sun Y P, Gel'mukhanov F, Kosugi N and Miron C 2013 Single-molecule x-ray interferometry: controlling coupled electron-nuclear quantum dynamics and imaging molecular potentials by ultrahigh-resolution resonant photoemission and *ab initio* calculations *Phys. Rev. X* **3** 011017
- [40] Eckert S et al 2018 One-dimensional cuts through multidimensional potential-energy surfaces by tunable x rays *Phys. Rev. A* **97** 053410
- [41] Reinhard S 1993 *Photodissociation Dynamics: Spectroscopy and Fragmentation of Small Polyatomic Molecules* (Cambridge Monographs on Atomic, Molecular and Chemical Physics) (Cambridge: Cambridge University Press)
- [42] Gel'mukhanov F and Ågren H 1996 X-ray resonant scattering involving dissociative states *Phys. Rev. A* **54** 379–93
- [43] Pietzsch A et al 2011 Spatial quantum beats in vibrational resonant inelastic soft x-ray scattering at dissociating states in oxygen *Phys. Rev. Lett.* **106** 153004
- [44] Felicissimo V C, Minkov I, Guimarães F F, Gel'mukhanov F, Cesar A and Ågren H 2005 A theoretical study of the role of the hydrogen bond on core ionization of the water dimer *Chem. Phys.* **312** 311–8
- [45] Liu J-C, Vaz da Cruz V, Polyutov S, Föhlisch A and Gel'mukhanov F 2019 Recoil-induced dissociation in hard-x-ray photoionization *Phys. Rev. A* **100** 053408
- [46] Gel'mukhanov F and Ågren H 1996 Raman, non-Raman, and anti-Raman dispersion in resonant x-ray scattering spectra of molecules *Phys. Rev.* **54** 3960–70
- [47] Feifel R et al 2000 Observation of a continuum–continuum interference hole in ultrafast dissociating core-excited molecules *Phys. Rev. Lett.* **85** 3133